FTD-ID(RS)T-1327-83

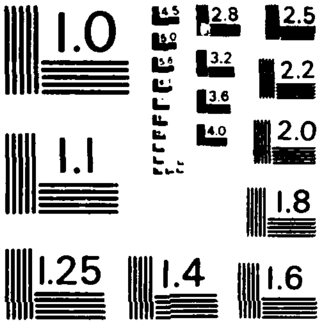

MICROCOPY RESOLUTION TEST CHART
NATIONAL BUREAU OF STANDARDS-1963-A

(2)

FTD-ID(RS)T-1927-83

FOREIGN TECHNOLOGY DIVISION

AIR FORCE SYSTEMS COMMAND

ACTA MECHANICA SINICA
(Selected Articles)

CORRECTED COPY

EDITED TRANSLATION

FTD-ID(RS)T-1927-83 1 May 1984

MICROFICHE NR: FTD-84-C-000447

ACTA MECHANICA SINICA (Selected Articles)

English pages: 20

Source: Lixue Xuebao, Nr. 4, 1983, pp. 414-418,
419-425

Country of origin: China
translated by: LEO KANNER ASSOCIATES
F33657-81-D-0264
Requester: FTD/TQTA
Approved for public release; distribution unlimited.

THIS TRANSLATION IS A RENDITION OF THE ORIGINAL FOREIGN TEXT WITHOUT ANY ANALYTICAL OR EDITORIAL COMMENT. STATEMENTS OR THEORIES ADVOCATED OR IMPLIED ARE THOSE OF THE SOURCE AND DO NOT NECESSARILY REFLECT THE POSITION OR OPINION OF THE FOREIGN TECHNOLOGY DIVISION.	PREPARED BY: TRANSLATION DIVISION FOREIGN TECHNOLOGY DIVISION WP-AFB, OHIO.

CONTENTS

Page No.

THE OBSERVATIONS OF TURBULENT BOUNDARY LAYER COHERENT STRUCTURES IN AN ADVERSE GRADIENT FLOW

Lian Jixiang

Beijing Aeronautical Engineering College

The observations were made by hydrogen bubble method in a water channel 6.8 m long by 0.4 m wide and 0.3 m deep. A flat plate 6 m long was set along one side of the channel. After the observations of TBL structures in zero pressure gradient flow, a curved wall was set opposite to this plate to form a two-dimensional convergent-divergent passage as shown in Fig. 1. There were small separated bubbles appearing intermittently at $x = 200$ to 300 mm but no separation in the downstream part. Plate 1 is a plane view of TBL on this flat plate in zero pressure gradient flow taken at $y^+ = 8.4$, $R_\theta = 1200$. Plate 2 to 6 are the plane views and the side views of TBL on this same flat plate in the divergent passage at $x = 100$ to 300 mm and $y = 1$ to 4 mm. In this adverse pressure gradient flow the low speed spots (regions where the hydrogen bubble lines are dense) are as wide as the high speed spots as shown in Plate 2, 3, 4, while in the zero pressure gradient flow the low speed regions are narrow streaks (usually called low speed streaks) as shown in Plate 1. In the interior of a low speed spot (also high speed spot) the hydrogen bubble lines were uniform and smooth, there was no trace of chaotic flow. Generally the chaotic flow appeared only at one of the two side edges of each low speed spot, at the chaotic side the hydrogen bubble lines concentrated into a narrow dense white long streak with distorted non-smooth edges and hydrogen bubbles were diffused from there, while at the opposite side the hydrogen bubble lines remained smooth. The different flow features of the two side edges of each low speed spot were shown clearly in Plate 2, 3, 4. These dense white long streaks extended far down-stream and were similar to those streaks in zero pressure gradient flows. The side views show many large transverse vortices. In Plate 5 fluid at 'A' was raised up and at 'C' was pushed down to wall by a vortex. In Plate 6 the fluid at 'A' was farther from the bubble wire than the free stream part of the same hydrogen bubble line, therefore it should have flowed faster than the free stream.

This paper was received in April 1982.

I. Preface

The coherent structure of turbulent flow is an active branch of study originated in the past (more than) ten years in the study of turbulent flow; the branch plays a key role in understanding the origination regime of turbulent flow. There are quite a few papers comprehensively assessing and describing the coherent structure [1-4] of the boundary layer. There have been many papers studying the coherent structure of the turbulent boundary layer with zero pressure gradient; however, there are few papers dealing with the adverse pressure gradient. Flow of the adverse pressure gradient and separation of the boundary layer caused by adverse pressure are very important flow phenomena, related (for example) to stall of aircraft wings. Kline et al. [5] and Simpson et al. [6] conducted observations of the adverse pressure zone on the turbulent boundary layer; however, there have been no reports of graphs of coherent structure. This experiment was conducted on a two-dimensional diffusion sector in a water channel using the hydrogen bubble method. The paper emphasizes the description of observation results in the maximum gradient zone of adverse pressure; the boundary layer of the zone is close to separation. At the beginning of the diffusion sector used by Simpson et al. [6], the diffusion angle is close to zero. The diffusion angle along the flow direction gradually increases; the boundary layer is entirely separated in the middle portion of the diffusion sector. In this experiment, the diffusion angle is the greatest at the beginning of the diffusion sector; the angle gradually decreases along the flow direction (refer to Fig. 1). During experiments, the diffusion angle should increase as much as possible, so that the boundary layer is close to separation at the beginning of the diffusion sector. Since the boundary layer at the beginning sector is thinnest, a relatively high gradient of adverse pressure is feasible; thus, no separation occurs at the boundary layer at the end of the diffusion sector. Hence, the flow field is relatively stable, providing convenience in observation. The observed coherent structure is significantly different from the coherent structure of a turbulent boundary layer without adverse pressure gradient.

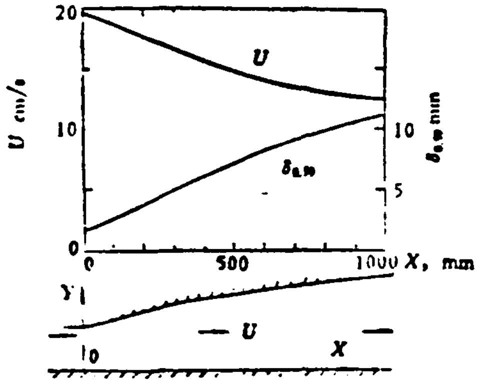

Fig. 1. Flow speed of free stream and boundary layer thickness in the diffusion sector and the shape of the sector.

II. Experimental Equipment and Method

The water channel is 6.8 meters long and 0.4 meter wide and high; the channel is made of organic glass. Near the lateral wall of the water channel, an organic-glass plate (6 m long, 0.3 m wide and 25 mm thick) was erected. First, observations on turbulent boundary layer without pressure gradient were conducted on the plate. Then, a curved wall was erected near another lateral wall of the channel. A two-dimensional convergent-divergent passage is thus formed between the plate and the curved wall. The width at the beginning of the divergent sector is 0.15 m; at a distance of 4.5 m from the front edge of the flat plate, the diffusion sector is 1 m long. At the end, the diffusion sector is 0.32 m wide. Refer to Fig. 1 for the shape of the diffusion sector; in the figure, x is the distance from the cross section of the inlet of the diffusion sector. y is the distance from the surface of the flate-plate wall.

The hydrogen bubble method used can give a graph of turbulent structure. A platinum wire, 25 μm in diameter, as the hydrogen-bubble-producing filament, was placed in water for observation. The cathode of a power source is connected with the platinum filament, and the anode is placed in water in a non-interference flow field; the power source is square-wave pulsed electricity. Its voltage and frequency can be adjusted. During experimentation, the frequency is fixed at 9.1 Hz. According to the flow speed of the observation zone and the length of the platinum filament, the voltage can be determined; in this experiment, the voltage used was 15 to 150 V. A 1 KW projection lamp was used for illumination. Under the action of pulsed electricity on the platinum filament, hydrogen bubbles were formed in streaks. Each pulse produces a streak of hydrogen bubbles, called the hydrogen bubble versus time line. If the platinum filament is marked with coated paint or a pressure trace with equal intervals, the equidistant markings also form hydrogen-bubble streaks; this is called the hydrogen bubble versus time dyed line. All these methods were used in the experimentation.

In this experiment, the water depth of the water channel was 0.3 m; the flow speed at the inlet of the diffusion sector was 19.2 cm/sec. The distribution of flow speeds in the diffusion sector is shown in Fig. 1. The observation proceeded on the flat-plate side in the diffusion sector; the front edge of the flat plate is the turning axis. The platinum filament was made to be perpendicular to the flat plate; the formed hydrogen-bubble streaks were generally situated above plane xy. The observation from the lateral surface (along the x axis) is called the lateral-surface observation; structures like a vortex-shaped movement can be observed within the boundary layer. The platinum filament was made parallel to the flat plate and perpendicular to the free stream; the hydrogen-bubble streaks thus formed are generally parallel to the wall surface. The observation from the direction perpendicular to the flat plate is called the front-side observation; images of high-speed spots, low-speed spots and streaks can be seen at the bottom layer of the boundary layer.

In the side-view photograph, the interval of two hydrogen-bubble streaks closest to the platinum filament represents the instantaneous flow speed at the place. By using a microscope coordinate instrument, the distance between the two front edges of the hydrogen-bubble streaks can be measured; at the same time, the dimension markings on the measurement negative are measured. The actual interval between two hydrogen-bubble streaks is then obtained by proportional conversion; the actual length is then divided by the time interval between two pulses to obtain the instantaneous flow velocity at the place. From this method, the pattern of instantaneous velocity of the boundary layer can be obtained; then the mean velocity pattern can be derived. For details of this method, refer to papers [7 and 8]. By using this method in experiments, the flow velocity U of the free stream in the diffusion section, and the distribution of thickness $\delta_{.99}$ (of the boundary layer) along the x axis can be obtained. In addition, a hot-membrane velocity-measuring instrument (of 50 μm diameter) is used to conduct the same measurement; the distribution of U and $\delta_{.99}$ are shown in Fig. 1.

III. Experimental Results

For comparison, first observation of the coherent structure of a turbulent boundary layer of zero pressure gradient is conducted. Then, observation is conducted at the same flat plate for the gradient of adverse pressure caused by the installation of a curved wall; the obtained coherent structural graph of the turbulent flow is significantly different from that of the zero pressure gradient. In the sector from x=100 mm to x=300 mm, the gradient of adverse pressure is greatest. There are some outstanding characteristics for the turbulent-flow structure. In the following, the description is emphasized of the observation results of this sector (simply called the beginning sector).

From a series of front- and side-view graphs observed within the turbulent boundary layer of a flat plate of zero pressure gradient, the results are generally consistent with the results obtained by Kline et al. [5] and Kim et al. [7]. Photograph 1 of plate I is a front-view graph of the experiment; the photograph shows the major structural images of fast-speed spots (within the zone of sparse hydrogen-bubble-time streaks), low-speed spots (within the zone of dense hydrogen-bubble-time streaks), and streaks (long white streaks formed downstream of the block of spots by hydrogen bubbles, generally along the direction of the free stream). In photograph 1 of plate I, hydrogen-bubble-time streaks are used; these streaks are different from the hydrogen-bubble-time dyed lines (equal-interval coated paint markings on the platinum filament) used by Kline et al. [5]. In appearance, these two graphs are different. However, by examining them closely, the characteristics of the two, in that they show the fast-speed spots, low-speed spots and streaks on the shapes and the mean-interval between streaks (z^+ at approximately 100), are consistent. However, in the paper the images of fast-speed, low-speed spots and streaks shown by hydrogen-bubble-time streaks are clearer. The streak graphs shown by the two-cases are generally consistent.

The x-direction width of low-speed spots in a zero-pressure gradient is very narrow. Even at places very close to the wall surface (y^+=3.3 as achieved by the author and his colleagues), the width of low-speed spots is much smaller than that of fast-speed spots. Therefore, the shape of low-speed spots is generally narrow streaks along the stream direction. At the beginning sector of the experiment, the x-direction width of low-speed spots is close to or exceeds the fast-spot width, as shown by photographs 2 through 4 in plate I. Therefore, all graphs of low-speed and high-speed spots are spots of large area. Compared to the zero pressure gradient, the hydrogen-bubble streaks within low-speed spots are denser, and the difference in densities of hydrogen-bubble streaks of the low-speed spots and fast-speed spots is greater. This is because the flow speed within low-speed spots is lower. The low-speed spots become wider and thicker, and the flow velocity within the spots is lower; these are characteristics for a boundary layer close to separation. This further lowers the flow speed within the low-speed spots; even the flow speeds become negative values, thus forming reverse-flow spots (a divergent bubble). In the middle portion of photograph 4 of plate I, there are a few hydrogen-bubbles flowing to the upper stream of the platinum filament; this is a reverse-flow spot. In the beginning sector within the zone of x=200 mm to 300 mm, small reverse-flow spots generally appear intermittently, revealing the closeness of divergence of the boundary layer at the place. Therefore, in the paper, the dimensionless wall surface units (such as y^+ and z^+) are not used to indicate the experimental data in the adverse pressure zone.

Since the low-speed spots are wider, we can clearly discriminate the flow images inside the low-speed spots and their edge. We can see from photographs 2 through 4 in plate I that the distribution of hydrogen-bubble streaks in low-speed spots is relatively even, like that inside the high-speed spots. Intervals between streaks are changed moderately along the Z direction; this indicates that the flow velocities within spots are relatively even. The relatively high velocity-gradient appears in the transitional zone at the junction point of low-speed and high-speed spots. From photographs 2 through 4 in plate I, and thousands of pictures and films photographed by the author and his colleagues, we can see that for two lateral edges of a low-speed spot, generally only one side is rapidly transferred into a fast-speed spot; on the other side, it is moderately transferred to a fast-speed spot. At the lateral edge of moderate transition, the intervals of hydrogen-bubble streaks generally change from dense to sparse, forming a wider transition belt. The curve of each hydrogen-bubble streak is smooth with its edge clearly visible, without a trace of chaotic flow. At the side of fast transition, the intervals of hydrogen-bubble streaks are rapidly becoming smaller. Not far from downstream of the platinum filament, all hydrogen-bubble streaks converge densely together, forming a long, slender and dense white streak; this narrow streak separates the fast-speed and low-speed spots; the transcendent streak has a very high velocity gradient. This white streak generally extends along the flow direction toward downstream, as indicated by " " on photograph 2 of plate I; the shape is not much different from the streak of the bottom layer of a zero pressure gradient. We can see that the edge of these streaks is not smooth, with hydrogen bubbles diverging from the edge; the streaks are twisted or divergent downstream. These graphs indicate turbulent motion. We can also see by comparing these graphs the following: the slower the low-speed spots (in other words, the denser the hydrogen-bubble streaks), the more chaotic are the streaks at the side. By visual observation, direction vortices frequently appear at the side edge of the rapid transition zone. From the right side of the reverse-flow spots of photograph 4 of plate I, the streaks are spiral shaped; downstream, there is a large conic vortex. There is no chaotic flow at the side of moderate

By observing the lateral surface of the beginning sector, in the majority of photographs there are transverse vortex motions, but very few vortices along the flow direction. This phenomenon is different from that of a zero pressure gradient. In the observation results by Kim et al. [7] on the lateral surface of a turbulent boundary layer of zero pressure gradient, there are mostly flow-direction vortices, estimated as two thirds of all vortices and one third of the lateral-direction vortices. At the beginning sector, there are many large lateral-direction vortices; it can be seen that these vortices exert an influence on the flow of most zones of the local boundary layer. In the second hydrogen-bubble streak (the hydrogen-bubble streak closest to the platinum filament is the first one, then in sequence toward the downstream in the order second, third, ...) of photographs 2 through 4 of plate I, the vortex center is about 5 mm from the wall surface. By its influence, the left lower terminal of the second hydrogen-bubble streak rises to A; its right side is lowered to C. In the photograph, B is the left lower terminal of the third hydrogen-bubble streak. Without the influence of this vortex, it should be close to the wall surface, but actually it rises, with only a narrow seam remaining with the sector AC of the second hydrogen-bubble streak. The induction of a lateral-direction vortex reduces the flow velocity while raising the flow at its lower rear side. In photograph 5, there is a gap in the lower terminal of the first hydrogen-bubble streak, indicating that the flow velocity is reduced, as it is influenced by the preceding vortex. The induction of a lateral-direction vortex on its upper front fluid shows relatively clearly in photograph 6 of plate I. In the photograph, A is situated at the right upper side of a lateral-direction vortex. At the place influenced by the vortex on the dyed streaks (the black streaks in the hydrogen-bubble streaks formed by pressure traces on the platinum filament), the hydrogen raising the fluid. This function of the lateral-direction vortex creates an exchange of momentum on a large scale.

IV. Conclusions

This paper presents the observation results of a two-dimensional divergent sector (the sector from x=100 mm to x=300 mm) in a water channel. This sector is the largest portion of the adverse pressure gradient of the pressure spreading sector. During experiments, a small number of divergent bubbles intermittently appear, indicating the closeness of divergence. However, downstream from this sector, there are no divergent bubbles. Compared to the zero pressure gradient, the main characteristics of the structure of the turbulent boundary layer are wide low-speed spots and further lower flow velocity, more difference from the flow speed of high-speed spots; there are many large transverse vortices. Since the low-speed spots are wider, the flow can be clearly discriminated between the inside and the edge of the low-speed spots. Within the low-speed and high-speed spots, the flows are relatively homogeneous and steady; at the same time, the other side is chaotic. The hydrogen-bubble streaks of the steady side are smooth and clear with a wider transitional zone between the high-speed spots. In the chaotic side, the hydrogen-bubble streaks are dense, becoming a beam of a dense white streak. The edge of the streak is not smooth, with divergent hydrogen bubbles, or with traces of the chaotic motion, such as twisted shape or divergence. The streak extends far downstream; its shape is similar to the streak of a zero pressure gradient. In the quiet side, generally no streaks are formed; the transverse vortices are larger. The flow velocity in the vicinity of some vortices is apparently greater than the flow velocity outside the local boundary layer.

LITERATURE

[1] **Kline. S. J., Falco, R. E. AFOSR-TR-80-0290(1980).**

[2] **Willmarth, W. W., et al., *Phys. Fluids* 20(1977). s9—s21**

3. Cai Shutang and Zhou Guangtong, Lixue Jinzhan [Progress in Mechanics], 10, 1 (1980).

[4] Comte-Bellot, G. AGARD CP 291(1980), 1—34.
[5] Kline, S. J., et al., *J. Fluid Mech.* 30(1967), 741.
[6] Simpson, R. L., et al., *J. Fluid Mech.*, 79(1977), 535
[7] Kim, H. T., et al., *J. Fluid Mech.*, 50(1970), 133.
[8] Schraub, F. A. et al., *J. Basic Eng.*, 87(1965), 429.

THREE-DIMENSIONAL TURBOMACHINE TRANSONIC FLOW EQUATIONS AND CHARACTERISTIC THEORY EXPRESSED WITH RESPECT TO NON-ORTHOGONAL CURVILINEAR COORDINATES

Lu Wenqiang

Institute of Engineering Thermophysics, Chinese Academy of Sciences

By the use of tensor calculus, three-dimensional turbomachine transonic flow equations in weak-conser-vative form, time-dependent iterative equations of two kinds of fluid surface and characteristic theory expressed with respect to non-orthogonal curvilinear coordinates have been derived in this paper.

This paper uses tensor calculus to derive the three-dimensional weak conservation form equations, time dependent flow surface iterative equations, and characteristic theory of non-orthogonal curvilinear coordinates. These equations and theory are valuable in solving the three-dimensional transonic flow field (with shock wave) of turbomachines, in addition to numerical analysis of circumferential- and diametral-direction anomalies, and for calculating the trembling vibration unsteady aerodynamic force.

1. Three-dimensional weak conservation form equations of non-orthogonal curvilinear coordinates

The non-orthogonal curvilinear coordinate three-dimensional flow equations [2] of turbomachines are

---

This paper was received on 4 May 1982.

$$\frac{\partial(\rho\sqrt{g})}{\partial t} + \frac{\partial}{\partial x^i}(\rho\sqrt{g}\,w^i) = 0 \tag{1}$$

$$\frac{\partial w_1}{\partial t} - w^2\left[\frac{\partial w_2}{\partial x^1} - \frac{\partial w_1}{\partial x^2}\right] + w^3\left[\frac{\partial w_1}{\partial x^3} - \frac{\partial w_3}{\partial x^1}\right] - 2\sqrt{g}\,(w^2\omega^3 - w^3\omega^2)$$

$$= -\frac{\partial I}{\partial x^1} + T\frac{\partial S}{\partial x^1} \tag{2}$$

$$\frac{\partial w_2}{\partial t} - w^3\left[\frac{\partial w_3}{\partial x^2} - \frac{\partial w_2}{\partial x^3}\right] + w^1\left[\frac{\partial w_2}{\partial x^1} - \frac{\partial w_1}{\partial x^2}\right] - 2\sqrt{g}\,(w^3\omega^1 - w^1\omega^3)$$

$$= -\frac{\partial I}{\partial x^2} + T\frac{\partial S}{\partial x^2} \tag{3}$$

$$\frac{\partial w_3}{\partial t} - w^1\left[\frac{\partial w_1}{\partial x^3} - \frac{\partial w_3}{\partial x^1}\right] + w^2\left[\frac{\partial w_3}{\partial x^2} - \frac{\partial w_2}{\partial x^3}\right] - 2\sqrt{g}\,(w^1\omega^2 - w^2\omega^1)$$

$$= -\frac{\partial I}{\partial x^3} + T\frac{\partial S}{\partial x^3} \tag{4}$$

$$\frac{\partial I}{\partial t} + w^i\frac{\partial I}{\partial x^i} - \frac{1}{\rho}\frac{\partial p}{\partial t} = 0 \tag{5}$$

By using the relationship equation:

$$-\nabla I + T\nabla S = -\frac{1}{\rho}\nabla p - \nabla\frac{1}{2}[(W)^2 - (\omega r)^2];$$

$$w_i = \sqrt{g_{ii}}\,W^i\cos\theta_{ij}; \quad w^i = \frac{W^i}{\sqrt{g_{ii}}}$$

and $(2)\times\rho\sqrt{g} + (1)\times w_1$; $(3)\times\rho\sqrt{g} + (1)\times w_2$;

$(4)\times\rho\sqrt{g} + (1)\times w_3$; $(5)\times\rho\sqrt{g} + (1)\times I$

We then derive the three-dimensional weak conservation form equations:

$$\frac{\partial U}{\partial t} + \frac{\partial F}{\partial x^1} + \frac{\partial G}{\partial x^2} + \frac{\partial H}{\partial x^3} = K \tag{6}$$

$$U = \begin{pmatrix} \rho\sqrt{g} \\ \rho\sqrt{g}\,w_1 \\ \rho\sqrt{g}\,w_2 \\ \rho\sqrt{g}\,w_3 \\ \rho\sqrt{g}\,I - p\sqrt{g} \end{pmatrix} \qquad F = \begin{pmatrix} \rho\sqrt{g}\,w^1 \\ \rho\sqrt{g}\,w_1w^1 + p\sqrt{g} \\ \rho\sqrt{g}\,w_2w^1 \\ \rho\sqrt{g}\,w_3w^1 \\ \rho\sqrt{g}\,I w^1 \end{pmatrix}$$

$$G = \begin{pmatrix} \rho\sqrt{g}\, w^2 \\ \rho\sqrt{g}\, w_1 w^2 \\ \rho\sqrt{g}\, w_2 w^2 + p\sqrt{g} \\ \rho\sqrt{g}\, w_3 w^2 \\ \rho\sqrt{g}\, I w^2 \end{pmatrix} \qquad H = \begin{pmatrix} \rho\sqrt{g}\, w^3 \\ \rho\sqrt{g}\, w_1 w^3 \\ \rho\sqrt{g}\, w_2 w^3 \\ \rho\sqrt{g}\, w_3 w^3 + p\sqrt{g} \\ \rho\sqrt{g}\, I w^3 \end{pmatrix} \qquad K = \begin{pmatrix} 0 \\ a_1 \\ a_2 \\ a_3 \\ 0 \end{pmatrix}$$

$$a_1 = p\,\frac{\partial\sqrt{g}}{\partial x^1} + \rho\sqrt{g}\left\{ w^i W^j \frac{\partial}{\partial x^1}\left(\sqrt{g_{ii}}\cos\theta_{ij}\right) + \frac{1}{2} W^i W^j \frac{\partial\cos\theta_{ij}}{\partial x^1} + (\omega)^2 r \frac{\partial r}{\partial x^1} + 2\sqrt{g}\left(w^2\omega^3 - w^3\omega^2\right)\right\}$$

$$a_2 = p\,\frac{\partial\sqrt{g}}{\partial x^2} + \rho\sqrt{g}\left\{ w^i W^j \frac{\partial}{\partial x^2}\left(\sqrt{g_{ii}}\cos\theta_{ij}\right) + \frac{1}{2} W^i W^j \frac{\partial\cos\theta_{ij}}{\partial x^2} + (\omega)^2 r \frac{\partial r}{\partial x^2} + 2\sqrt{g}\left(w^3\omega^1 - w^1\omega^3\right)\right\}$$

$$a_3 = p\,\frac{\partial\sqrt{g}}{\partial x^3} + \rho\sqrt{g}\left\{ w^i W^j \frac{\partial}{\partial x^3}\left(\sqrt{g_{ii}}\cos\theta_{ij}\right) + \frac{1}{2} W^i W^j \frac{\partial\cos\theta_{ij}}{\partial x^3} + (\omega)^2 r \frac{\partial r}{\partial x^3} + 2\sqrt{g}\left(w^1\omega^2 - w^2\omega^1\right)\right\}$$

2. Time dependent flow surface iterative equations

The author and his colleagues derived fundamental equations (along the flow surface) on the curvilinear coordinate system (x^1, x^2, x^3, x^4) fixed at the rotating shaft of turbomachines. In the fundamental equations, $x^4=t$ and the basic vector $J_i = \partial r/\partial x^i$.

In the space, there is an unsteady flow surface $x^3=x^3(x^1, x^2, t)$.

For the normal and tangential direction dot product of the flow surface:

$$\boldsymbol{n}\cdot d\boldsymbol{r} = n_i dx^i = \frac{N_i}{\sqrt{\bar{g}^{ii}}}\, dx^i = 0$$

In the equation,

$$\bar{g}_{ij} = \boldsymbol{J}_i\cdot\boldsymbol{J}_j;\quad \bar{g}_{ij}\bar{g}^{jl} = \delta_i^l;\quad i,j = 1,2,3,t$$

(1) Continuity equations

At an instant, by taking any element of the flow surface with the measurement $d\bar{s} = \sqrt{a}\, dx^1 dx^2$; and by prescribing the area density σ of the flow sector, then the flow mass on an element of flow-sector surface is

$$\sigma d\bar{s} = \sigma \sqrt{a}\, dx^1 dx^2.$$

According to the law of conservation of mass and Reynolds' transmission theory, we obtain

$$\frac{d_m}{dt} \iint_{\bar{s}(t)} \sigma d\bar{s} = \iint_{\bar{s}(t)} \tau \frac{\partial \sigma}{\partial t} + \mathrm{div}(\sigma \boldsymbol{W}) d\bar{s} = 0$$

and then

$$\frac{\partial \sigma}{\partial t} + \mathrm{div}(\sigma \boldsymbol{W}) = 0$$

Since the aforementioned computations proceeded at a flow surface, in order to discriminate the conventional computation, the following form of the equation is written:

$$\frac{\partial(\rho\tau\sqrt{a})}{\partial t} + \frac{\partial(\rho\tau w^i \sqrt{a})}{\partial x^i} = 0 \qquad (7)$$

In the equation, the thickness (of the flow sector) is $\tau = \rho/\sigma = (\sqrt{g}/\sqrt{a})dx^3$

(2) Momentum equations

In order to cancel out the partial derivatives in the x^3 direction, the relationship W·n=0 is applied in addition to the following calculations:

$$\frac{\bar{\partial} q}{\bar{\partial} x^k} = \frac{\partial q}{\partial x^k} + \frac{\partial q}{\partial x^3}\frac{\partial x^3}{\partial x^k} = \frac{\partial q}{\partial x^k} - \frac{n_k}{n_3}\frac{\partial q}{\partial x^3} \quad k = 1, 2,$$

Canceling out derivatives along the x^3 direction in equations (2), (3) and (4), we then obtain:

$$\frac{\bar{\partial} w_1}{\bar{\partial} t} - w^2\left[\frac{\bar{\partial} w_2}{\bar{\partial} x^1} - \frac{\bar{\partial} w_1}{\bar{\partial} x^2}\right] - w^3 \frac{\bar{\partial} w_3}{\bar{\partial} x^1} - 2\sqrt{g}(w^2\omega^3 - w^3\omega^2)$$
$$= -\frac{\bar{\partial} I}{\bar{\partial} x^1} + T\frac{\bar{\partial} S}{\bar{\partial} x^1} + f_1$$
$$\frac{\bar{\partial} w_2}{\bar{\partial} t} + w^1\left[\frac{\bar{\partial} w_2}{\bar{\partial} x^1} - \frac{\bar{\partial} w_1}{\bar{\partial} x^2}\right] - w^3 \frac{\bar{\partial} w_3}{\bar{\partial} x^2} - 2\sqrt{g}(w^3\omega^1 - w^1\omega^3)$$
$$= -\frac{\bar{\partial} I}{\bar{\partial} x^2} + T\frac{\bar{\partial} S}{\bar{\partial} x^2} + f_2$$

$$\frac{\partial w_3}{\partial t} + w^1 \frac{\partial w_3}{\partial x^1} + w^2 \frac{\partial w_3}{\partial x^2} - 2\sqrt{g}\,(w^1\omega^2 - w^2\omega^1) = f_3 \qquad (8)$$

$$f = -\frac{1}{n_3}\left(\frac{1}{\rho}\frac{\partial p}{\partial x^3} - (\omega)^2 r\,\frac{\partial r}{\partial x^3} + \frac{W^i W^j}{2}\frac{\partial \cos\theta_{ij}}{\partial x^3} - W^i W^j \cos\theta_{ij}\,\frac{\partial \ln\sqrt{g_{ii}}}{\partial x^3}\right) n$$

(3) Time dependent flow surface iterative weak conservation form equations

Processing Eqs. (7) and (8) as in section 1, we then obtain the time dependent flow surface iterative weak conservation form equations

$$\frac{\partial A}{\partial t} + \frac{\partial B}{\partial x^1} + \frac{\partial C}{\partial x^2} = D \qquad (9)$$

$$A = \begin{pmatrix} \rho\tau\sqrt{a} \\ \rho\tau\sqrt{a}\,w_1 \\ \rho\tau\sqrt{a}\,w_2 \\ \rho\tau\sqrt{a}\,w_3 \end{pmatrix} \qquad B = \begin{pmatrix} \rho\tau\sqrt{a}\,w^1 \\ \rho\tau\sqrt{a}\,w_1 w^1 + p\tau\sqrt{a} \\ \rho\tau\sqrt{a}\,w_2 w^1 \\ \rho\tau\sqrt{a}\,w_3 w^1 \end{pmatrix}$$

$$C = \begin{pmatrix} \rho\tau\sqrt{a}\,w^2 \\ \rho\tau\sqrt{a}\,w_1 w^2 \\ \rho\tau\sqrt{a}\,w_2 w^2 + p\tau\sqrt{a} \\ \rho\tau\sqrt{a}\,w_3 w^2 \end{pmatrix} \qquad D = \begin{pmatrix} 0 \\ \beta_1 \\ \beta_2 \\ \beta_3 \end{pmatrix}$$

$$\begin{aligned} \beta_1 = {} & p\tau\sqrt{a}\,\frac{\partial(\ln\tau\sqrt{a})}{\partial x^1} + \rho\tau\sqrt{a}\,(\omega)^2 r\frac{\partial r}{\partial x^1} + \rho\tau\sqrt{a}\,f_1 \\ & + 2\sqrt{g}\,\rho\tau\sqrt{a}\,(w^2\omega^3 - w^3\omega^2) + \rho\tau\sqrt{a}\,w^1 W^j\,\frac{\partial(\sqrt{a_{11}}\cos\theta_{1j})}{\partial x^1} \\ & - \frac{1}{2}\rho\tau\sqrt{a}\,W^i W^j\,\frac{\partial\cos\theta_{ij}}{\partial x^1} \end{aligned}$$

$$\begin{aligned} \beta_2 = {} & p\tau\sqrt{a}\,\frac{\partial(\ln\tau\sqrt{a})}{\partial x^2} + \rho\tau\sqrt{a}\,(\omega)^2 r\frac{\partial r}{\partial x^2} + \rho\tau\sqrt{a}\,f_2 \\ & + 2\sqrt{g}\,\rho\tau\sqrt{a}\,(w^3\omega^1 - w^1\omega^3) + \rho\tau\sqrt{a}\,w^2 W^j\,\frac{\partial(\sqrt{a_{22}}\cos\theta_{2j})}{\partial x^2} \\ & - \frac{1}{2}\rho\tau\sqrt{a}\,W^i W^j\,\frac{\partial\cos\theta_{ij}}{\partial x^2} \end{aligned}$$

$$\beta_3 = 2\rho\tau\sqrt{a}\sqrt{g}\,(w^1\omega^2 - w^2\omega^1) + f_3\rho\tau\sqrt{a}$$

In the equations, the steady state energy equation (dI/dt=0) is used for the energy equation, as expressed by numerical experiments, thus saving time in reaching the steady state.

3. Characteristic theory

The characteristic theory describes the objective rule of message exchange between the boundary and the internal flow field. By using the boundary conditions established by the characteristic theory, the time progressing process of numerical solution can be ensured with the reliable mathematical basis of physics.

Equations (7), (8) and equations of unsteady, cohesionless and adiabatic energy equations

$$\frac{\partial p}{\partial t} + w^i \frac{\partial p}{\partial x^i} = c^2 \left[\frac{\partial \rho}{\partial t} + w^i \frac{\partial \rho}{\partial x^i} \right]$$

are condensed and combined into

$$\sum_{K=1}^{5} a_\mu^K \cdot \mathrm{grad}\, u_K = b_\mu \quad K, \mu = 1, 2, 3, 4, 5$$

The aforementioned equations are combined linearly

$$\sum_{\mu=1}^{5} \sigma^\mu \sum_{K=1}^{5} a_\mu^K \cdot \mathrm{grad}\, u_K = \sum_{\mu=1}^{5} \sigma^\mu b_\mu$$

If we assume the normal direction (of the characteristic cone)

$$\lambda = \lambda_j e^j \qquad j = t,\ 1,\ 2$$

Then we have the characteristic equation

$$|\lambda_j a_\mu^{Kj}| = |A_{\mu K}| = 0 \tag{10}$$

The characteristic compatibility relationship is

$$\sum_{\mu=1}^{5} \sigma^\mu \sum_{K=1}^{5} a_\mu^K \cdot \mathrm{grad}\, u_K = \sum_{\mu=1}^{5} \sigma^\mu b_\mu \tag{11}$$

In the equation, α^{μ} is a root of the equation

$$\alpha^{\mu}(A_{K\mu}) = 0 \qquad (12)$$

(1) Characteristic equation

$$\begin{aligned}|A_{\mu K}| = &-D^{3}\tau\sqrt{g}\sqrt{g_{11}}\sqrt{g_{22}}\sqrt{g_{33}}[\cos^{2}\theta_{12}+\cos^{2}\theta_{23}-2\cos\theta_{12}\cos\theta_{23}\cos\theta_{13}\\ &-1+\cos^{2}\theta_{13}]-C^{2}D^{3}\tau\sin\theta_{13}\sqrt{g_{22}}[2\lambda_{1}\lambda_{3}\sqrt{g_{11}}\sqrt{g_{33}}(\cos\theta_{12}\cos\theta_{23}\\ &-\cos\theta_{13})-g_{11}(\lambda_{3})^{2}\cos^{2}\theta_{13}-g_{33}(\lambda_{1})^{2}\cos^{2}\theta_{23}+g_{33}(\lambda_{1})^{2}+g_{11}(\lambda_{3})^{2}]\\ &= D^{3}\tau\sin\theta_{13}\frac{g}{\sqrt{g_{22}}}\{-D^{2}+C^{2}\}=0\end{aligned} \qquad (10)^{*}$$

We then obtain the following characteristic types:

a. $D=\lambda\cdot W=0$ streamline; b. $D^{2}=C^{2}$ sonic-wave envelope.

(2) The characteristic compatibility relationship of the non-orthogonal curvilinear coordinate system

a. If we substitute $D=0$ into Eq. (12), we then obtain the following flow characteristic compatibility relationship:

The solution of the first group: $\alpha^{2}A_{24}+\alpha^{3}A_{34}=0$ momentum equation combination;

The solution of the second group: $\alpha^{3}=0$ $\alpha^{5}\neq 0$ energy equation

b. If we substitute $D^{2}=C^{2}$ into Eq. (12), we then obtain

$$\alpha^{1}=C^{2};\qquad \alpha^{2}=-\rho\tau\sqrt{g}D\lambda^{3};\qquad \alpha^{3}=-\rho\tau\sqrt{g}D\lambda^{2};$$
$$\alpha^{4}=0;\qquad \alpha^{5}=\tau\sqrt{g}$$

If we substitute the aforementioned equations into Eq. (11), we then obtain the wave characteristic compatibility relationship:

$$
\begin{aligned}
&C^2\tau\rho\frac{\sqrt{a}}{\sqrt{a_{11}}}\frac{\partial W^i}{\partial x^i}+\tau\sqrt{a}\left\{\frac{\partial \rho}{\partial t}+w^i\frac{\partial \rho}{\partial x^i}\right\}-\rho\tau\sqrt{a}\,D\lambda^1\left\{\sqrt{a_{11}}\left(\frac{\partial W^1}{\partial t}+w^i\frac{\partial W^1}{\partial x^i}\right)\right.\\
&\quad\left.+\sqrt{a_{11}}\cos\theta_{12}\left(\frac{\partial W^2}{\partial t}+w^i\frac{\partial W^2}{\partial x^i}\right)+\frac{1}{\rho}\frac{\partial p}{\partial x^1}\right\}-\rho\tau\sqrt{a}\,D\lambda^2\left\{\sqrt{a_{22}}\cos\theta_{12}\left(\frac{\partial W^1}{\partial t}\right.\right.\\
&\quad\left.\left.+w^i\frac{\partial W^1}{\partial x^i}\right)+\sqrt{a_{22}}\left(\frac{\partial W^2}{\partial t}+w^i\frac{\partial W^2}{\partial x^i}\right)+\frac{1}{\rho}\frac{\partial p}{\partial x^2}\right\}+\bar{F}=0
\end{aligned}
\tag{13}
$$

$$
\begin{aligned}
\bar{F}=\;&C^2\left[\rho\frac{\partial(\tau\sqrt{a})}{\partial t}+\rho W^i\frac{\partial(\tau\sqrt{a}/\sqrt{a_{11}})}{\partial x^i}\right]-\rho\tau\sqrt{a}\,D\lambda^1\left\{w^2\left[W^i\left(\frac{\partial(\sqrt{a_{11}}\cos\theta_{1i})}{\partial x^2}\right.\right.\right.\\
&\left.\left.-\frac{\partial(\sqrt{a_{22}}\cos\theta_{2i})}{\partial x^1}\right)\right]-2\sqrt{g}\,(w^2\omega^3-w^3\omega^2)-\frac{W^3}{\sqrt{g_{33}}}W^i\frac{\partial(\sqrt{g_{33}}\cos\theta_{i3})}{\partial x^1}\\
&\left.+\frac{1}{2}W^iW^j\frac{\partial\cos\theta_{ij}}{\partial x^1}-(\omega)^2r\frac{\partial r}{\partial x^1}-f_1\right\}\\
&-\rho\tau\sqrt{a}\,D\lambda^2\left\{w^1\left[W^i\left(\frac{\partial(\sqrt{a_{22}}\cos\theta_{2i})}{\partial x^1}-\frac{\partial(\sqrt{a_{11}}\cos\theta_{1i})}{\partial x^2}\right)\right]\right.\\
&+2\sqrt{g}\,(w^1\omega^3-w^3\omega^1)-(\omega)^2r\frac{\partial r}{\partial x^2}-f_2+\frac{1}{2}W^iW^j\frac{\partial\cos\theta_{ij}}{\partial x^2}\\
&\left.-\frac{W^3}{\sqrt{g_{33}}}W^i\frac{\partial(\sqrt{g_{33}}\cos\theta_{i3})}{\partial x^2}\right\}
\end{aligned}
$$

By using the characteristic theory at the boundary, and conducting a similar discussion like paper [2], we obtain the corresponding relationship. For three-dimensional equations (6), a similar method can be used to derive the characteristic theory of non-orthogonal curvilinear coordinates, and to conduct the corresponding discussion at boundaries.

4. Conclusion

(1) The introduction of non-orthogonal curvilinear coordinates can allow us to select the most suitable and practical curved lattice for a complex shaped blade grid and different types of flow problems in order to raise the

calculation accuracy and convergent speed. This compensates shortcomings in the old time-dependent method where arbitrary curve lattices cannot be formed. This is the reason that in the early 1980s, the body-fitted coordinate system was applied in several transonic numerical methods [3-5] abroad. At the appointed revolving S_1 surface, we conducted preliminary numerical experiments [2]. Our work shows that the application of non-orthogonal curvilinear coordinates in the time dependent method is successful.

(2) Ways of solving the three-dimensional transonic flow field (with shock wave) of turbomachines had been preliminarily studied abroad. For example, in [6] which applied the weak conservation form equation of a three-dimensional cylindrical coordinate system by selecting the MacCormack time-splitting format, in the space, first proceed with time increments along the r direction, and then the ϕ direction, and finally time increments along the z direction. The three-dimensioanl transonic flow field was obtained by using large amounts of computer time. In manuscripts [7] and [8], the time dependent iteration is similar to S_1-S_2 (two types of flow surface) of the cylindrical coordinate system. By using less computer time, the three-dimensional approximate flow field of the cylindrical coordinate system can be obtained which is comparable to experiments. We consider that the strict time dependent two-category flow surface iterative method can have time increments of the region to be solved, approximating the restraint of the flow surface. Obtaining the complete three-dimensional solution of the entire flow field is completed with the establishment of the steady-state solution of various groups of flow surfaces, and the iterative convergent solution of two groups of flow surfaces. This allows the skillful application of time increments of a single group of flow surfaces, and an alternate iteration technique of two groups of flow surfaces. Of course, the advantages and disadvantages of the two aforementioned methods of solving the three-dimensional flow field are subject to comparative numerical experiments.

The author expresses his thanks to Professor Wu Zhonghua for his counsel and support in this research work.

LITERATURE

1. Wu Zhonghua, Three-dimensional Turbomachine Flow Equations Expressed With Respect to Non-orthogonal Curvilinear Coordinates and Methods of Solution, Yanjiu Zhaji [Research Notes] (1963) Proceedings of Third ISABE, 1976, pp. 233-252, Munich 1976.

2. Lu Wenqiang and Chen Xuming, The S_1 Revolving Surface Transonic Flow Time Dependent Numerical Solution Using Non-orthogonal Curvilinear Coordinates and Non-orthogonal Velocity Component, Gongcheng Rewuli Xuebao [Journal of Thermophysics], 4, 2 (1983).

[3] Camerero, R., Younist, M.. Efficient generation of body-fitted coordinates for cascades using multigrid. *AIAA. J.* 18, 5(1980).

[4] Deconick. H., Hirsch. ch., Finite element methods for transonic blade-to-blade calculation in turbomachines, ASME 81-GT-5.

[5] Younist, M. E., Camerero, R.. Finite volume method for blade-to-blade flow using a body-fitted mesh. *AIAA. J.*, 19. 11(1981).

[6] Haymann-Haber, G., Thompkins, W. T., Comparison of experimental and computational shock structure in a transonic compressor rotor. *Transaction of ASME, A. Journal of Engineering for power*, 103. 1(1980).

[7] McDonald, P. W., Bolt. C. R., Dunker, R. J., Weyer. H. B., A comparison between measured and computed flow fields in a transonic compressor rotor, ASME 80-GT-7.

[8] Spurr, A., The prediction of 3-D transonic flow in turbomachinery using a combined throughflow and blade-to-blade time marching method, *Int. J. Heat and Fluid Flow*, 2, 4(1980).

END

FILMED

7-84

....) of photographs 2 through 4 of plate I, the vortex center is about 5 mm from the wall surface. By its influence, the left lower terminal of the second hydrogen-bubble streak rises to A; its right side is lowered to C. In the photograph, B is the left lower terminal of the third hydrogen-bubble streak. Without the influence of this vortex, it should be close to the wall surface, but actually it rises, with only a narrow seam remaining with the sector AC of the second hydrogen-bubble streak. The induction of a lateral-direction vortex reduces the flow velocity while raising the flow at its lower rear side. In photograph 5, there is a gap in the lower terminal of the first hydrogen-bubble streak, indicating that the flow velocity is reduced, as it is influenced by the preceding vortex. The induction of a lateral-direction vortex on its upper front fluid shows relatively clearly in photograph 6 of plate I. In the photograph, A is situated at the right upper side of a lateral-direction vortex. At the place influenced by the vortex on the dyed streaks (the black streaks in the hydrogen-bubble streaks formed by pressure traces on the platinum filament), the hydrogen bubble streaks have turned about 45° along the clockwise direction. At the place, the hydrogen-bubble streaks are farther from the platinum filament than the portion of the same hydrogen-bubble streak outside the boundary layer. This indicates that within the duration (about two pulse periods) from the platinum filament, the flow velocity of the hydrogen-bubble streak near the wall is greater than the flow velocity of the free stream. Apparently, this is the result of induction by the vortex. In many photographs, the lateral-direction vortices speed up the fluid at its upper front side to let the fluid descend, and reduce the velocity of the fluid in the rear downward side by